Chapter 4

Experimental Measurement of Phase Noise in NEMS

We present the experimental measurement of phase noise of NEMS. First, we analyze control servo behavior of the phase-locked loop, and give expressions for the locked condition and loop dynamics. We then describe two implementation schemes at very high frequency and ultra high frequency bands: (1) homodyne detection phase-locked loop based on a two port NEMS device and (2) frequency modulation phase-locked loop. The achieved phase noise and Allan deviation are compared with the local oscillator requirement of chip scale atomic clocks to evaluate the viability for such applications. Finally, we investigate the diffusion noise arising from the xenon atoms adsorbed on the NEMS surface by putting a ~190 MHz nanomechanical resonator into a phase-locked loop and measure the frequency noise and Allan deviation.

4.1 Introduction

We have presented the theory of phase noise mechanism of NEMS in chapter 3. So far, to our knowledge, none of *fundamental* noise sources proposed has been measured and very little experimental results are available to decide whether the predicted noise performance of NEMS can indeed be achieved. In this chapter, we address this problem by inserting high *Q* NEMS resonators in phase-locked loops and evaluate their noise performance against controlled variations in their environments.

We start our discussion from analyzing control servo behavior of a general phase-locked loop scheme based on NEMS and give the expressions for the locked condition and loop bandwidth. We then present two electronic implementations of NEMS-based phase-locked loops: (1) homodyne phase-locked loop based on a two port NEMS device and (2) frequency modulation phase-locked loop (FM PLL). These phase-locked loops are designed to lock minute electromechanical resonance of NEMS embedded in a large electrical background as a result of diminishing transducer responsivity as the device dimensions are scaled downward. The achieved noise floor in terms of phase noise density and Allan deviation will be compared with the local oscillator (LO) requirement of chip scale atomic clock (CSAC) to evaluate the viability of NEMS oscillators for this application.[1,2]

Finally, we investigate the diffusion noise arising from the xenon atoms adsorbed on the NEMS surface and measure the corresponding frequency noise and Allan deviation using FM PLL. We will characterize the adsorption behavior, extract the diffusion coefficients, and compare the experimental results with diffusion noise theory and Yong and Vig's model, both described in chapter 3.

4.2 Analysis of Phase-Locked Loop Based on NEMS

In general, two categories of schemes are commonly used for phase noise measurement: self-oscillation and phase-locked loop (PLL). In the self-oscillation scheme depicted in figure 4.1, the resonator operates within a positive feedback loop. The phase noise, manifesting itself in the noise sideband around the carrier, is measured by a spectrum analyzer (see section 2.3). The Allan deviation is calculated from the data taken with the frequency counter. Such a scheme has widely been used to characterize oscillators, and the detailed analysis can be found elsewhere.[3]

In this work, we extensively use the phase-locked loop scheme shown in figure 4.2(a). The principal elements of the loop are voltage control oscillator (VCO) and the resonant response circuitry. The VCO is simply an oscillator whose frequency is proportional to an externally applied voltage. The response function circuitry, containing NEMS and phase detection circuitry, produces a quasi-dc signal proportional to the phase of the mechanical resonance of NEMS. This phase sensitive signal is usually passed through a loop filter, then applied to the control input of the VCO, and serves as error signal to close the feedback loop. If the resonance frequency shifts slightly, the feedback will adjust the control voltage to track the frequency change. Therefore, the voltage fluctuation in the control input of the VCO reflects the frequency noise in the loop. Moreover, the Allan deviation can be obtained from the data taken with the frequency counter.

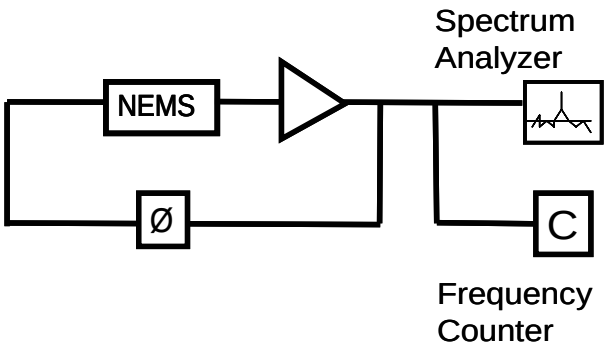

Figure 4.1. Self-oscillation scheme for the phase noise measurement of NEMS. The principal components of the self-oscillation scheme are (1) NEMS, (2) the amplifier, and (3) the phase shifter. The phase noise, manifesting itself in the noise sidebands around the carrier, is measured by a spectrum analyzer. The Allan deviation can be calculated from the data taken with the frequency counter.

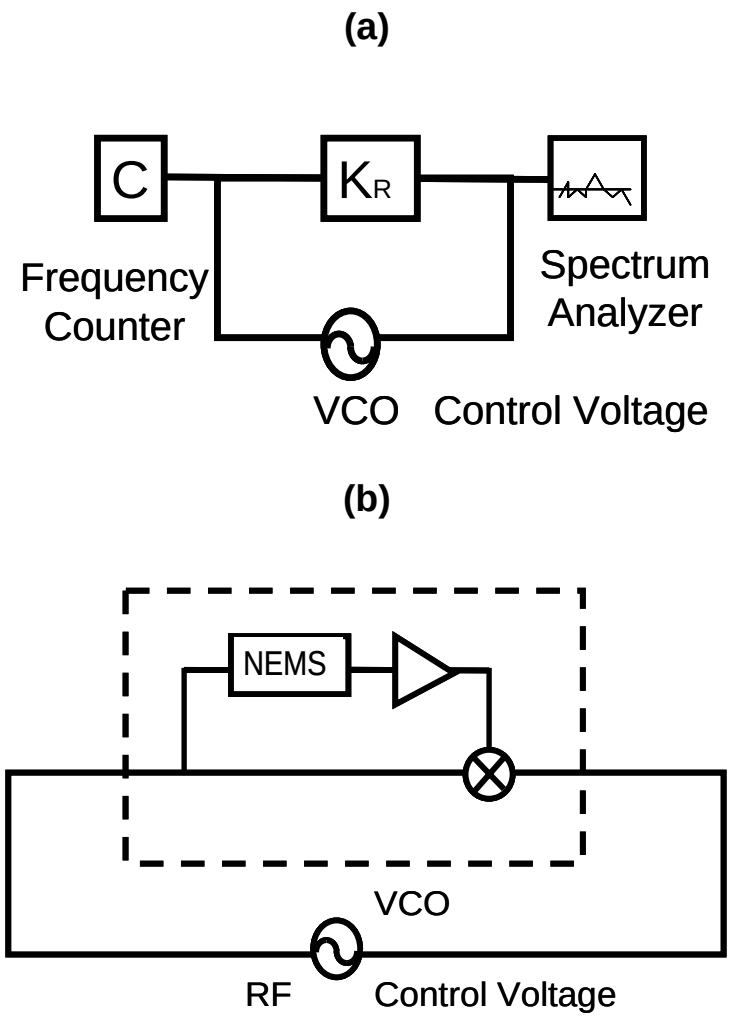

Figure 4.2. Configuration of a phase-locked loop based on NEMS. (a) Measurement scheme of a phase-locked loop (PLL) based on NEMS. The principal components of a PLL are the voltage controlled oscillator (VCO) and the resonant response circuitry (K_R). The output of the resonant response circuitry is used as error signal to the control input of the VCO to close the feedback loop. The frequency noise, manifesting itself as voltage fluctuation in the control port of the VCO, is measured by a spectrum analyzer. The Allan deviation is obtained from the data taken with frequency counter (C). **(b) Homodyne phase-locked loop.** Homodyne phase-locked loop is one example of the scheme shown in (a). In the homodyne phase detection, the NEMS device is driven by a VCO at constant amplitude, and the output is amplified and mixed with the carrier. The resonant response circuitry consists of NEMS, the amplifier, and the mixer.

We now analyze control servo behavior of the PLL, aiming to understand the locked condition and the loop dynamics under the feedback. The frequency of the VCO is determined by the control voltage $V_{control}$, as given by

$$\omega_{VCO} = \omega_{VCO}(V_{control} = 0) + K_V V_{control} . \quad (4.1)$$

K_V and $\omega_{VCO}(V_{control} = 0)$ are the frequency pulling coefficient and the center frequency of the VCO, respectively. The output of the resonant response circuitry can be represented as a voltage function of carrier frequency, $V_R(\omega_C)$, and is applied to the control input of VCO to provide the feedback. We analyze the loop behavior by linearizing $V_R(\omega_C)$ in the vicinity of the resonance frequency, ω_0, of the NEMS as

$$V_R(\omega_C) = K_R(\omega_0 - \omega_C) . \quad (4.2)$$

Here the proportional constant K_R, called henceforth the resonant response coefficient, is defined by $K_R = (\partial V_R / \partial \omega_C)_{\omega=\omega_0}$. When the VCO is locked to the NEMS, we have the condition $V_R = V_{control}$. From equation (4.1) and equation (4.2), we obtain the locked condition

$$\omega_C = \omega_{VCO}(V_{control} = 0) + K_V K_R(\omega_0 - \omega_C) . \quad (4.3)$$

We define the open loop gain of the PLL as

$$K_{loop} = K_V K_R . \quad (4.4)$$

Therefore, equation (4.3) can be rewritten as

$$\omega_C = \frac{K_{loop}}{1 + K_{loop}} \omega_0 + \frac{1}{1 + K_{loop}} \omega_{VCO}(V_{control} = 0) . \quad (4.5)$$

Assuming that VCO is infinitely stable, i.e., $\omega_{VCO}(V_{control} = 0)$ is constant, equation (4.5) implies that any frequency variation in the resonant frequency $\delta\omega_0$ of the device

will be scaled by a factor $K_{loop}/(1+K_{loop})$ as a result of feedback and reflected in the corresponding carrier frequency change $\delta\omega_C$ in the phase-locked loop, i.e.,

$$\delta\omega_C = \frac{K_{Loop}}{1+K_{Loop}}\delta\omega_0 . \tag{4.6}$$

Equation (4.5) also implies an experimental way to measure the loop gain K_{loop}. We rewrite equation (4.5) as

$$\omega_C - \omega_0 = \frac{1}{1+K_{loop}}(\omega_{VCO}(V_{control}=0)-\omega_0) . \tag{4.7}$$

In other words, $\omega_C - \omega_0$ is proportional to $\omega_{VCO}(V_{control}=0)-\omega_0$ with the proportionality constant $1/(1+K_{loop})$. Experimentally one can hold the resonant frequency ω_0 constant, rest the center frequency of VCO, $\omega_{VCO}(V_{control}=0)$, incrementally, and record the carrier frequency ω_C of the loop under lock. By plotting ω_C versus $\omega_{VCO}(V_{control}=0)$, we can determine the loop gain from the slope, i.e., the proportionality constant $1/(1+K_{loop})$.

So far we have considered the locked condition of the PLL in the steady state. We now analyze the loop dynamics and give the expressions for the loop bandwidth. We first discuss the case that a first-order low pass filter with a frequency cutoff, Δf_{filter}, described by the transfer function, $H_{filter}(\omega) = 1/(1+ j(\omega/2\pi\Delta f_{filter}))$, is employed in the control input of the VCO. Repeating the same steps from equation (4.1) to equation (4.5) by replacing K_V with $K_V H_{filter}$, we obtain

$$\omega_C = \frac{K_{loop}/(1+K_{loop})}{1+ j\omega/[(1+K_{loop})2\pi\Delta f_{filter}]}\omega_0 + \frac{1}{1+K_{loop}H_{filter}}\omega_{VCO}(V_{control}=0) . \tag{4.8}$$

Equation (4.8) means that the servo tracks the resonant frequency of the device with the loop bandwidth Δf_{PLL} given by

$$\Delta f_{PLL} = \Delta f_{filter}(1 + K_{loop}) . \tag{4.9}$$

Now we can write down the intrinsic bandwidth of the PLL limited by the NEMS itself. This is done by simply replacing Δf_{filter} in equation (4.9) with the resonant bandwidth $(\omega_0 / 2\pi Q)$ in the loop.[3] As a result, the intrinsic bandwidth of the PLL is given by

$$\Delta f_{PLL} = (\omega_0 / 2\pi Q)(1 + K_{loop}) . \tag{4.10}$$

Both equation (4.9) and equation (4.10) imply that the effect of feedback enhances the bandwidth by the factor $1 + K_{loop}$. For applications requiring fast response time, we can always increase the loop gain to extend the loop bandwidth. Similar ideas have also been used to enhance the bandwidth of atomic force microscopy by Albrecht et al.[3]

Finally, we give the explicit expression for the resonant response coefficient. The resonant response function, $V_R(\omega_C)$, is determined by the transducer voltage from NEMS, $V_{transducer}(\omega_C)$, cascaded by the amplifier gain, K_A, and the gain of phase detection circuitry, K_P, as given by

$$V_R(\omega_C) = V_{transducer}(\omega_C) K_A K_P . \tag{4.11}$$

Taking the derivative of the resonant response function with respect to the carrier frequency, the resonant response coefficient is given by

$$K_R \equiv (\partial V_R / \partial \omega_C)_{\omega_C = \omega_0} = (\partial V_{transducer} / \partial \omega)_{\omega_C = \omega_0} K_A K_P . \tag{4.12}$$

As an example, we give the expression of resonant response coefficient for homodyne phase-locked loop. The homodyne phase-locked loop shown in figure 4.2(b) is

one incarnation of the scheme shown in figure 4.2(a). In such a scheme, the NEMS device is driven by a VCO at constant amplitude and the output is amplified and mixed with the carrier. We first give the expression for the resonant response coefficient K_R. The gain of the phase detection circuitry K_P is given by the mixer gain K_M. $\partial V_{transducer} / \partial \omega_C$ can be approximated by $QV_{transducer}^{\max} / \omega_0$. $V_{transducer}^{\max}$ is the maximum transducer voltage producing linear response. Thus, the loop gain of the PLL is given by

$$K_R = K_M K_A Q V_{transducer}^{\max} / \omega_0 . \tag{4.13}$$

In the magnetomotive transduction, $V_{transducer}^{\max}$ is given by the electromotive force (emf) voltage generated across the device with length L vibrating with the amplitude $|x_C|$ at the frequency ω_0 in the magnetic field B, i.e.,

$$V_{transducer}^{\max} = BL\omega_0 |x_C| . \tag{4.14}$$

PLL	Frequency	Dimensions($L \times w \times t$)	Q	M_{eff}	DR	σ_A(1sec)	Δf
Two Port	125 MHz	1.6 μm × 800 nm × 70 nm	1300	1 pg	80 dB	4×10^{-7}	165 kHz
FM VHF	133 MHz	2.3 μm × 150 nm × 70 nm	5000	100 fg	80 dB	5×10^{-8}	32 Hz
FM VHF	190 MHz	2.3 μm × 150 nm × 100nm	5000	150 fg	80 dB	1×10^{-7}	32 Hz
FM UHF	419 MHz	1.35 μm × 150 nm × 70 nm	1000	50 fg	100 dB	1×10^{-7}	32 Hz

Table 4.1. Summary of parameters of all phase-locked loops based on NEMS presented in this work

4.3 Homodyne Phase-Locked Loop Based upon a Two-Port NEMS Device

We now present the electronic implementation of the homodyne phase-locked loop based on the scheme shown in figure 4.2(b) using a two port NEMS device, who parameters are summarized in table 4.1. In practice, the two port topology avoids direct electrical feedthrough of the simple one port scheme and allows careful design of the bonding fixture to minimize the unwanted parasitic coupling that produces a large electrical background on top of electromechanical resonance. Figure 4.3(a) shows the SEM micrograph of the two port device fabricated from SiC epilayer with Au metallization.[4] It is driven magnetomotively and the resonant frequency is found to be ~125 MHz with quality factor Q=1300. Figure 4.3(b) shows the fundamental mode of vibration of a two port device, optimized through the finite element simulation.

Figure 4.4 shows the electronic implementation of the PLL. The low phase noise VCO (Minicircuits POSA-138) drives the NEMS device at constant amplitude and the output of the transducer of the NEMS is amplified by a low noise preamplifier (Miteq AU1442). We further employ an external bridge, consisting of a variable phase shifter and a variable attenuator, to null out the electrical background. Figure 4.5 shows the resulting mechanical resonant response of the NEMS after the nulling. The rising background away from resonance shows the narrowband nature of the nullling, and hence the locking range of the loop is limited within the natural width of the resonance due the finite bandwidth of the variable phase shifter in the external bridge.The signal from the external bridge is then mixed down with the carrier, amplified by an instrumentation amplifier (Stanford Research Systems SR560), offset by a precision bias circuit, and fed into the control input of the VCO to close the feedback control loop. Note

that the cutoff frequency of the low pass filter in the control servo is set to 1 MHz to fully utilize the intrinsic bandwidth, $(1+K_{loop})(\omega_0/2\pi Q)$=165 kHz, provided by the NEMS device (K_{loop} approximately equals to 1). Hence this scheme is very desirable in sensing applications requiring fast response.

Figure 4.6 shows the phase noise spectrum of the VCO in PLL as measured by spectrum analyzer (Hewlett Packard HP8563E). At frequencies between 100 Hz and 20 kHz, the spectrum exhibits flicker noise and has $1/f^3$ dependence on the offset frequency due to the upconversion of the flicker noise of the preamplifier to the sideband of the carrier. Above 20 kHz, the spectrum flattens out to about -110dBc/Hz, the instrument noise floor of the spectrum analyzer.

Figure 4.7 shows the Allan deviation versus averaging times from frequency data over the course of ~1000 sec interval taken with the frequency counter. At the logarithmic scale, the observed Allan deviation, is nominally independent of averaging time and confirms the flicker noise in the phase noise spectrum. Note that the error bar of the each data point represents the confidence interval of the Allan deviation, given by $\sigma_A(\tau_A)/\sqrt{N_S-1}$. For τ_A= 1 sec, the observed Allan deviation $\sigma_A(\tau_A)$=4.7 x 10^{-7} is consistent with the estimated value 7.7 x 10^{-7} from the theoretical expression $\sigma_A(\tau_A)=(1/Q)10^{-DR/20}$ (with dynamic range DR=80 dB and Q=1300). In the present experiment, DR is limited by (extrinsic) transducer-amplifier noise and the onset of the Duffing instability of the NEMS device.

(a)

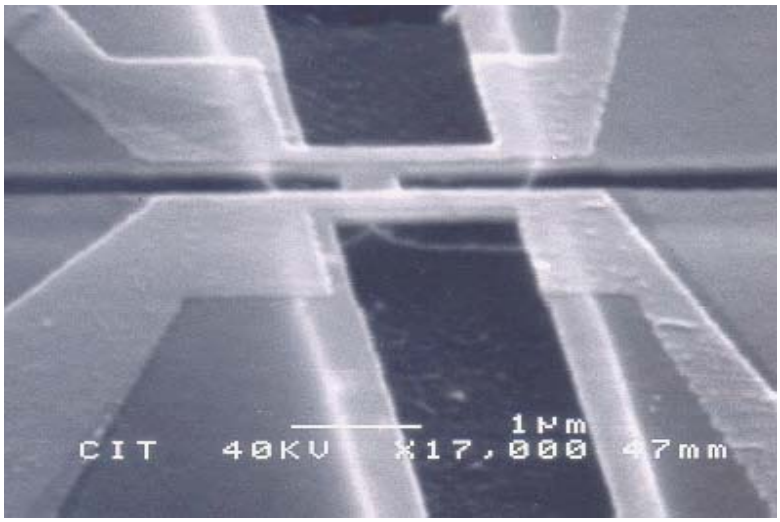

(b)

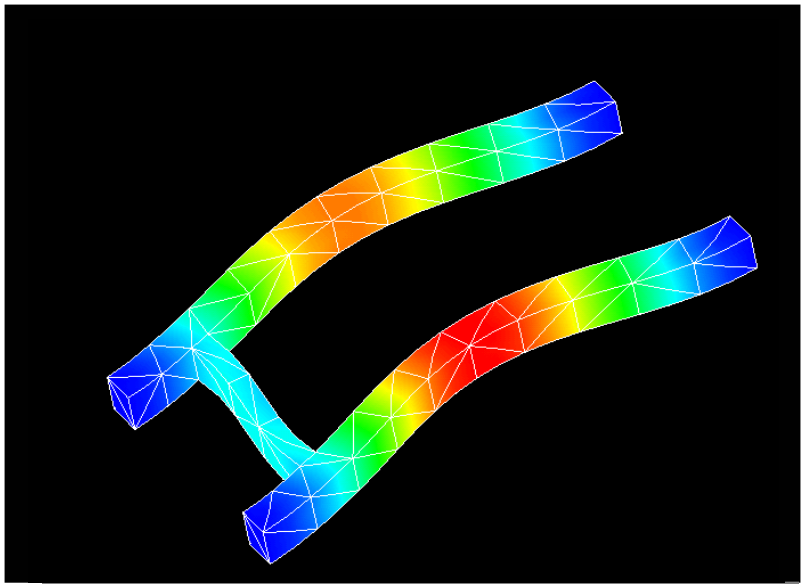

Figure 4.3. Pictures of two-port NEMS devices. (a) SEM micrograph of the two port NEMS device. The device is fabricated from SiC epilayer with Au metallization. **(b) Finite element simulation of the fundamental mode of vibration of a two port device.** The two port device consists of two doubly clamped beams mechanically coupled by a central beam. We use the finite element simulation to optimize the mechanical design.

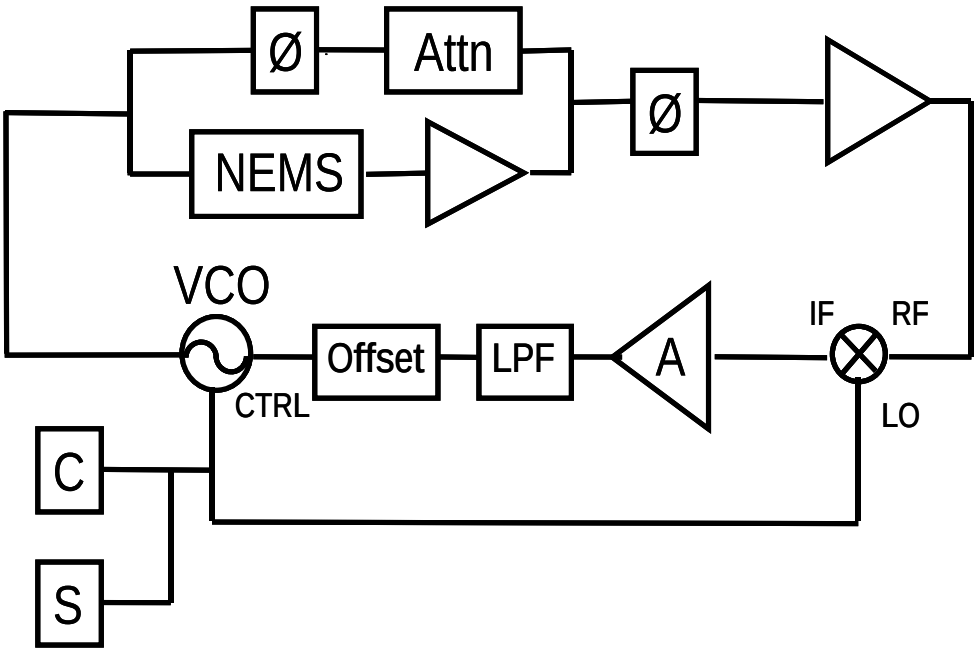

Figure 4.4. Implementation of the homodyne phase-locked loop based on a two-port NEMS device. We use a two port NEMS device with external bridge to implement the homodyne phase-locked loop. The external bridge, comprised of a narrowband voltage controlled phase shifter (ϕ) and a voltage controlled variable attenuator (Attn), is used to null the electrical background.

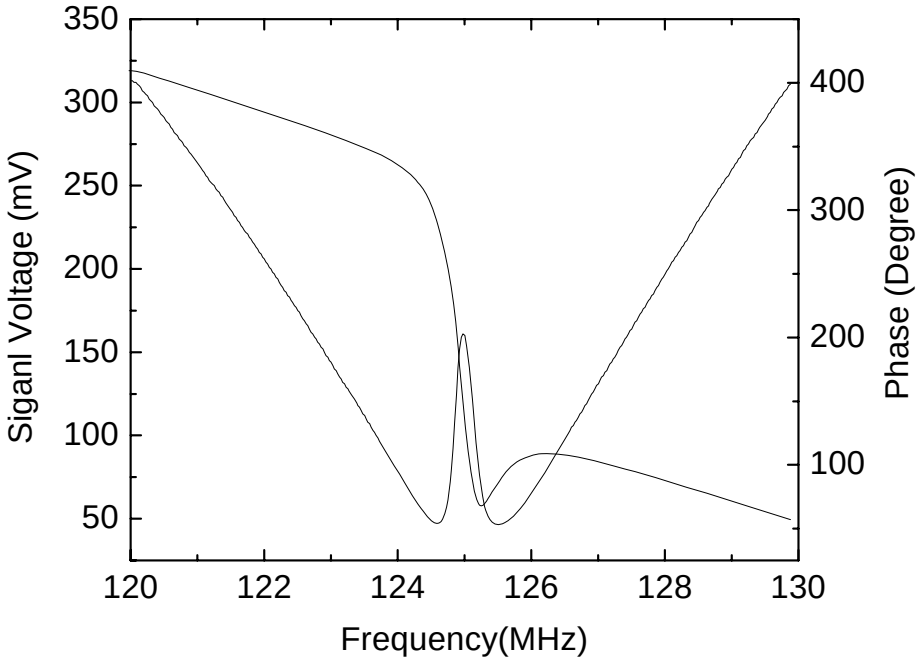

Figure 4.5. Mechanical resonant response after nulling. The mechanical resonance of the NEMS at 125 MHz is shown after the constant electrical background is nulled out by an external bridge circuit. The rising background away from resonance shows the narrowband nature of the nullling due to the bandwidth of the variable phase shifter in the external bridge. This limits our locking range within the natural width of the resonance.

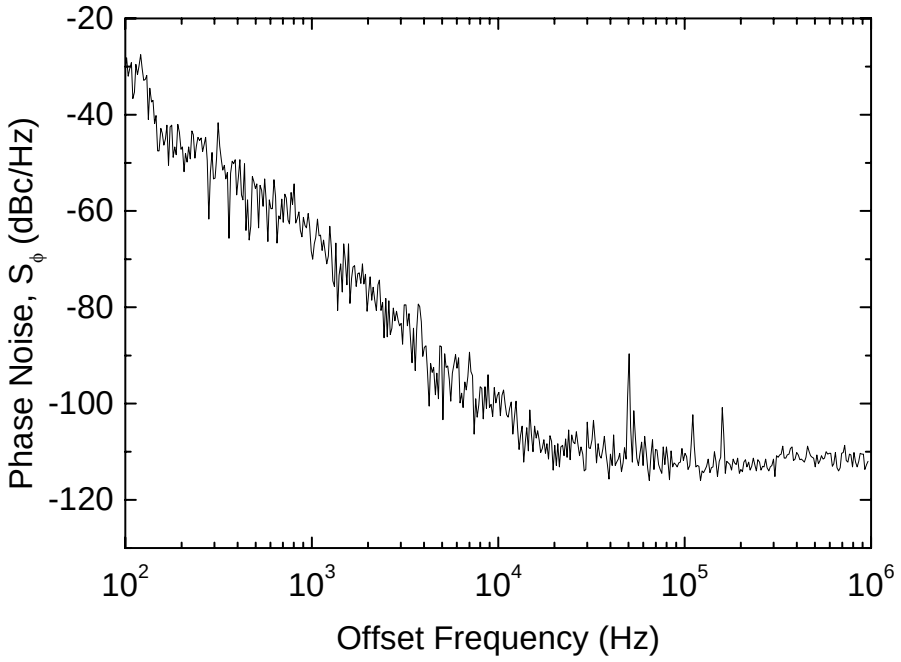

Figure 4.6. Phase noise density of the 125 MHz homodyne phase-locked loop based on a two-port NEMS device. The phase noise density of the 125 MHz homodyne phase-locked loop based on a two port NEMS is shown. Between 100 Hz and 20 kHz, the phase noise spectrum exhibits flicker noise, i.e., having $1/f^3$ dependence on the offset frequency. Above 20 kHz, it flattens out to ~110 dBc/Hz, the instrument noise floor of the spectrum analyzer.

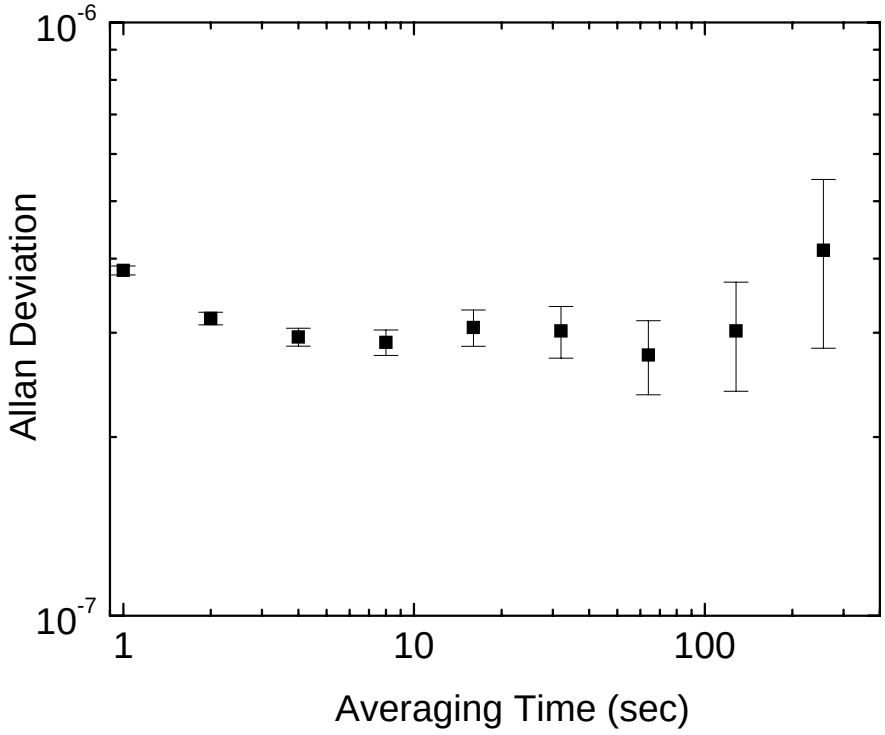

Figure 4.7. Allan deviation of the 125 MHz homodyne phase-locked loop based on a two-port NEMS device. The Allan deviation of 125 MHz homodyne phase-locked loop versus averaging time, calculated from frequency data over the course of ~1000 sec interval, is shown. At logarithmic scale, the Allan deviation is nominally independent of averaging time and consistent with the observed flicker noise in the phase noise spectrum in figure 4.6. The error bar in each data point represents the one-standard-deviation confidence interval of the Allan deviation.

4.4 Frequency Modulation Phase-Locked Loop

We now present the analysis and implementation of the frequency modulation phase-locked loop, which is designed to lock the even smaller electromechanical resonance of a NEMS embedded in a large electrical background. Roughly speaking, the frequency modulation of the carrier and subsequent demodulation by lock-in detection after mixer generates an electrical signal proportional to the derivative of the resonant response with respect to frequency. As a result, the constant electrical background, in which the electromechanical resonance of the NEMS is embedded, is nulled out. As shown in figure 4.8, the FM PLL is formed by adding frequency modulation of the carrier and lock-in detection to the homodyne phase-locked loop. One can prove that addition of the frequency modulation and lock-in detection contributes to K_R with two additional gain factors, the frequency modulation index M and the lock-in detection gain K_{Lockin}. By inserting these two factors into equation (4.13), we find

$$K_R = (K_M K_A Q V_{transducer}^{\max} / \omega_0) M K_{Lockin} . \tag{4.15}$$

Note that $M = V_m K_V / \omega_m$ in the case that a sinusoidal voltage of magnitude V_m at modulation frequency, ω_m is applied to the control voltage port of VCO.

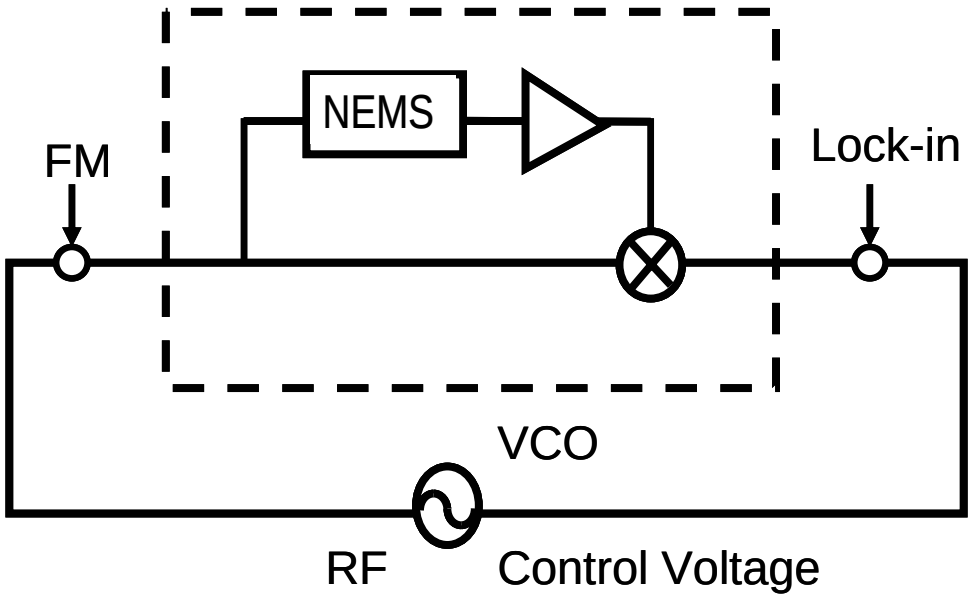

Figure 4.8. Conceptual diagram of frequency modulation phase-locked loop (FM PLL) scheme. Similar to homedyne phase-locked loop, the NEMS is driven by a VCO at constant amplitude, and the output is amplified and mixed with the carrier. The FM PLL is formed by adding the frequency modulation (FM) of the carrier and the lock-in detection to the homodyne phase-locked loop.

Figure 4.9 shows the electronic implementation of the FM PLL at VHF (very high frequency) band for 133 MHz and 190 MHz devices. The device configurations are summarized in table 4.1. We detect the mechanical resonance in the reflection scheme by a directional coupler. The signal from the NEMS device is amplified by a radio frequency (RF) amplifier with gain, K_{RF}, shifted in phase by the phase shifter, and subsequently mixed down to intermediate frequency (IF) by a mixer. The IF signal is further amplified by an IF amplifier with gain, K_{IF}. The total amplifier gain is given by

$$K_A = K_{RF} K_{IF} . \tag{4.16}$$

In our experiment, the carrier is modulated at 1.2652 kHz with reference oscillator in the lock-in amplifier. The lock-in amplifier (Stanford Research Systems SR830) is employed to detect the signal amplitude at the modulation frequency and subsequently rescale the readout according to the *Sensitivity* setting with full scale voltage $V_{fullscale}$. This is further divided by a voltage divider with a dividing factor *DF*. For convenience, we incorporate the voltage division and rescaling into the lock-in detection gain

$$K_{lockin} = (1/DF) V_{fullscale} / Sensitivity . \tag{4.17}$$

We summarize the experimental parameters used in FM PLL at 190 MHz in table 4.2. To close the feedback loop, the lock-in amplifier outputs the signal to the control port of the VCO. We use the frequency synthesizer (Hewlett Packard HP8648) in frequency modulation mode as the VCO. This imposes a proportional control with a frequency cutoff proportional to the inverse of the lock-in time constant τ_{lockin}. More precisely, the bandwidth of the FM PLL is given by $\Delta f_{PLL} = (1 + K_{loop})(1/2\pi\tau_{lockin})$ using equation (4.9) as a result of feedback. In addition, a digital feedback loop is established by a computer

interface, which periodically checks the digital output of the lock-in amplifier, computes a correction, and resets the center frequency of the VCO accordingly with prescribed loop gain and loop time. Effectively one has a discrete integral control, extending the locking range beyond the natural width of the resonance. We use it to follow the frequency shift induced by large changes in device mass over extended measurement intervals.

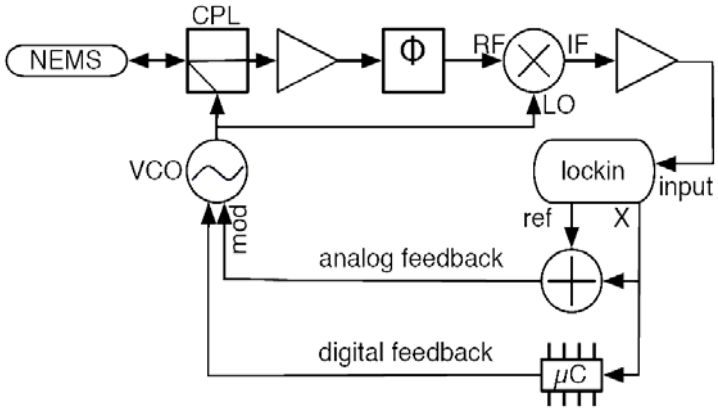

Figure 4.9. Implementation of frequency modulation phase-locked loop (FM PLL) scheme. We employ frequency modulation phase-locked loop (FM PLL) scheme to track the resonant frequency of the device. The mechanical resonance is detected in a reflection scheme, by using a directional coupler (CPL). The reflected signal is amplified, phase shifted (Φ), and mixed down (⊗). We modulate the carrier at 1.2652 kHz and employ a lock-in amplifier (Stanford Research Systems SR830) for demodulation. The resulting output (X) provides the analog feedback to the VCO (Hewlett Packard HP8648B). A computer-controlled parallel digital feedback (μC) is implemented for applications requiring a large locking range.

Figure 4.10 shows the phase noise spectrum of the FM PLL based on the 190 MHz device. At frequencies between 15 mHz and 30 Hz, the spectrum exhibits flicker noise, having $1/f^3$ dependence on the offset frequency. Above 30 Hz, the spectrum rolls off at the slope of 50 dB/decade, reflecting the loop bandwidth limited by the filter in lock-in detection. With the lock-in time constant τ_{lockin} = 10 ms and K_{loop} =1, we estimate the loop bandwidth to be 32 Hz from the expression $\Delta f_{PLL} = (1+K_{loop})(1/2\pi\tau_{lockin})$. Figure 4.11 shows the observed Allan deviation calculated from data over the course of one hour taken with frequency counter (Agilent 53132) for τ_A ranging from 1 sec to 128 sec. At the logarithmic scale, the observed Allan deviation versus averaging time is nominally constant and thus consistent with flicker noise in the phase noise spectrum in Figure 4.10. The Allan deviation $\sigma_A(\tau_A)$=1x10^{-7} for τ_A= 1 sec is close to the estimated value 2x10^{-7} from the expression $\sigma_A(\tau_A) = (1/Q)10^{-DR/20}$ (with dynamic range *DR* = 80 dB and *Q*= 5000).

We have also implemented the FM PLL at the ultra high frequency (UHF) band at 419 MHz. For the 419 MHz SiC device with dimensions 1.35 um(*L*) x 150 nm(*w*) x 70 nm (*t*) and *Q*=1600, the mechanical impedance is only ~0.08 Ω and embedded in a large electrical impedance ~100 Ω. To detect such a small impedance at the UHF band, we replace the simple reflection scheme used for FM PLL at the VHF band with a balanced bridge detection (see also chapter 7).[5] To amplify the signal from the NEMS device, we employ a cryogenic amplifier (Miteq AFS3-00100200-09-CR-4), working from 0.1 to 2 GHz with the equivalent noise temperature T_N =10 K at 419 MHz. We summarize the experimental parameters in table 4.2. Figure 4.12 shows the observed phase noise

spectrum. At frequencies between 15 mHz and 30 Hz, the spectrum exhibits $1/f^2$ dependence on the offset frequency. Similar to the FM PLL at VHF band, the additional rolloff in the spectrum at 30 Hz results from the loop bandwidth $\Delta f_{PLL} = (1 + K_{loop})(1/2\pi\tau_{lockin})$=32 Hz (with τ_{lockin} = 10 ms and K_{loop}=1). Figure 4.13 shows the Allan deviation calculated from the frequency data over the course of one hour taken with the frequency counter (Agilent 53132). For τ_A=1 sec, the observed Allan deviation σ_A=1 x 10^{-7} is much higher than the estimated value of 6.25 x 10^{-9} from the expression $\sigma_A(\tau_A) = (1/Q)10^{-DR/20}$ with *DR*=100 dB and *Q*=1000. (*DR* is estimated assuming the white noise contribution from the cryogenic amplifier with equivalent noise temperature T_N=10 K at 419 MHz and onset of Duffing nonlinearity of the NEMS.) We attribute this discrepancy to the conversion of other noise sources to side band of the carrier through the mixer or the nonlinearity of the circuit.

Table 4.2. Summary of experimental parameters used in the frequency modulation phase-locked loops (FM PLL) at very high frequency (VHF) and ultra high frequency (UHF) bands

Parameter	Symbol	VHF PLL	UHF PLL
Resonant Frequency	$\omega_0/2\pi$	190MHz	419MHz
Quality Factor	Q	5000	1600
Transducer Voltage	$V_{transucer}^{max}$	~1μV	~1μV
RF Gain	K_{RF}	35dB	45dB
IF Gain	K_{IF}	500	500
Mixer Gain	K_M	~0.1	~0.1
Modulation Frequency	$\omega_m/2\pi$	1.3kHz	10kHz
Modulation Voltage	V_m	30mV	30mV
Frequency Pulling Coefficient	K_V	100kHz/V	50kHz/V
Sensitivity	*Sensitivity*	200mV	1 mV
Dividing Factor	*DF*	10	10
Full Scale Voltage	$V_{fullscale}$	10V	10V
Lock-in Time Constant	$\tau_{lock\text{-}in}$	10ms	10ms
Modulation Index	M	2.3	0.15
Loop Gain (Estimated)	K_{loop}	~4.8	~4.5
Loop Gain (Measured)	K_{loop}	~1	~1

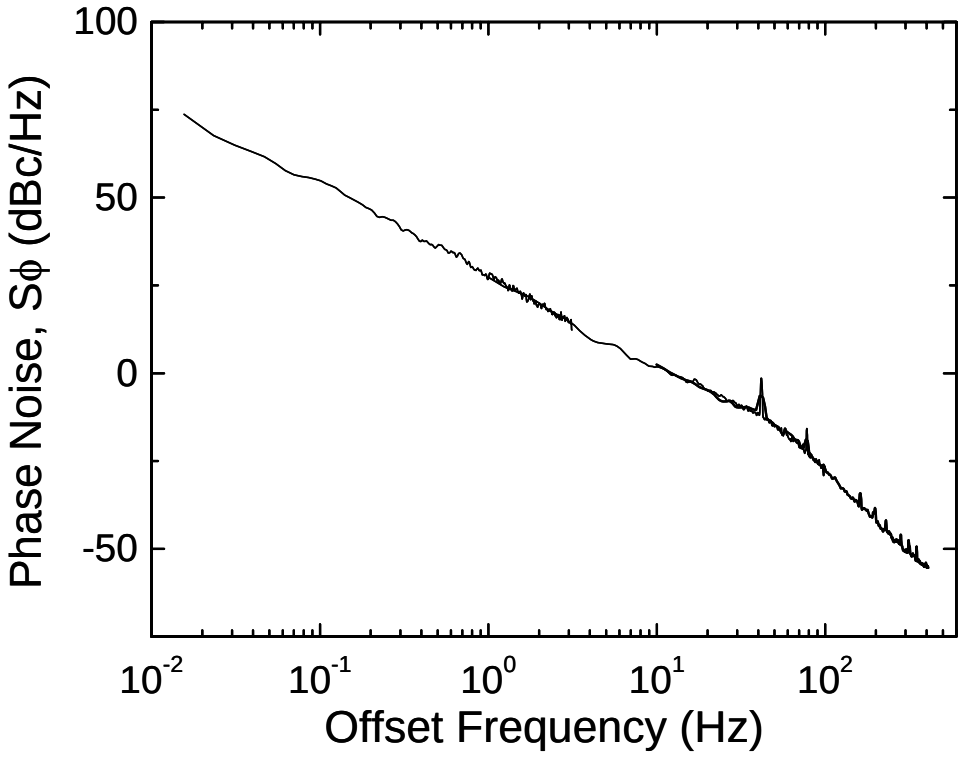

Figure 4.10. Phase noise density of the 190 MHz frequency modulation phase-locked loop (FM PLL). The phase noise density of the 190 MHz FM PLL is shown. Between 15 mHz and 30 Hz , the phase noise spectrum of the 190 MHz phase-locked loop exhibits flicker noise, i.e., having $1/f^3$ dependence on the offset frequency. Above 30 Hz, it rolls off at the slope of 50 dB/decade due to the loop bandwidth limited by lock-in detection $\Delta f_{PLL} = (1 + K_{loop})(1/2\pi\tau_{lock-in})$ =32 Hz (with $\tau_{lock-in}$ =10 ms and K_{loop} =1).

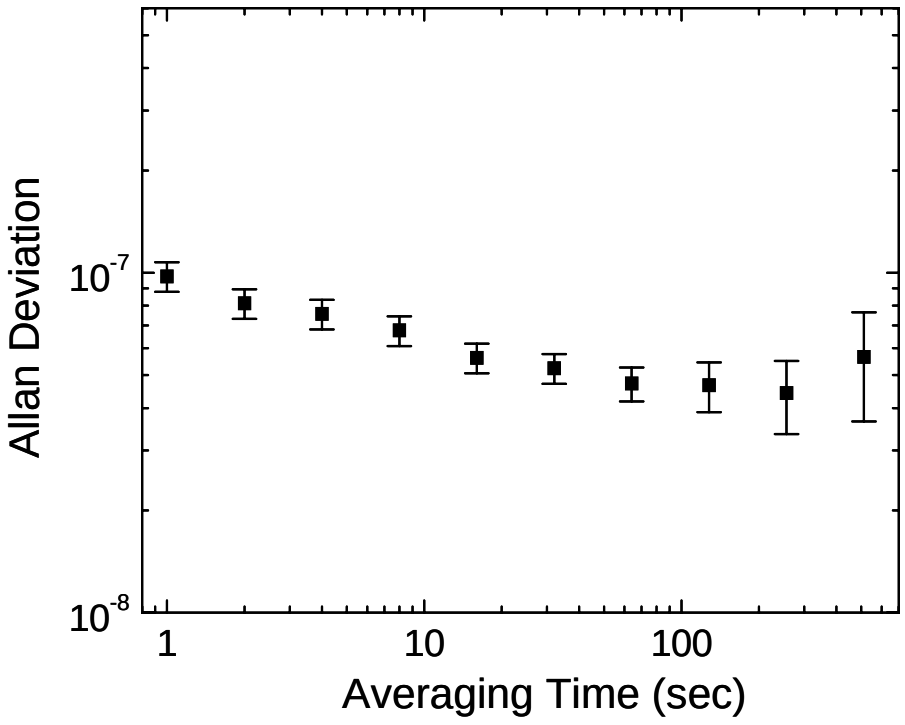

Figure 4.11. Allan deviation of the 133 MHz frequency modulation phase-locked loop (FM PLL). The Allan deviation of the 133 MHz FM PLL versus averaging time, calculated from frequency data over the course of one hour, is shown here. At logarithmic scale, the Allan deviation is nominally independent of averaging time and thus consistent with the observed flicker noise in the phase noise spectrum. The error bar in each data point represents the one-standard-deviation confidence interval of the Allan deviation.

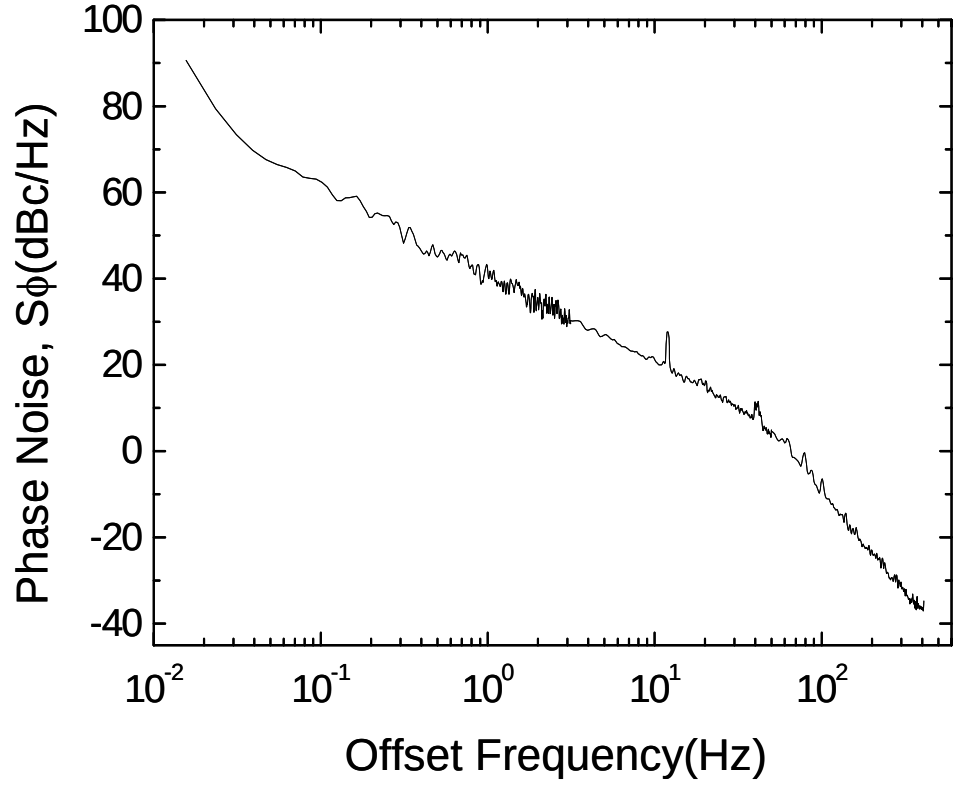

Figure 4.12. Phase noise density of the 419 MHz frequency modulation phase-locked loop (FM PLL). The phase noise density of the 419 MHz FM PLL is shown. Between 15 mHz and 30 Hz, the phase noise spectrum of the 419 MHz phase-locked loop exhibits white noise, having $1/f^2$ dependence on offset frequency. Above 30 Hz, it rolls off at the slope of 40 dB/decade due to the loop bandwidth limited by lock-in detection $\Delta f_{PLL} = (1 + K_{loop})(1/2\pi\tau_{lock-in})$ =32 Hz (with $\tau_{lock-in}$ =10 ms and K_{loop} =1).

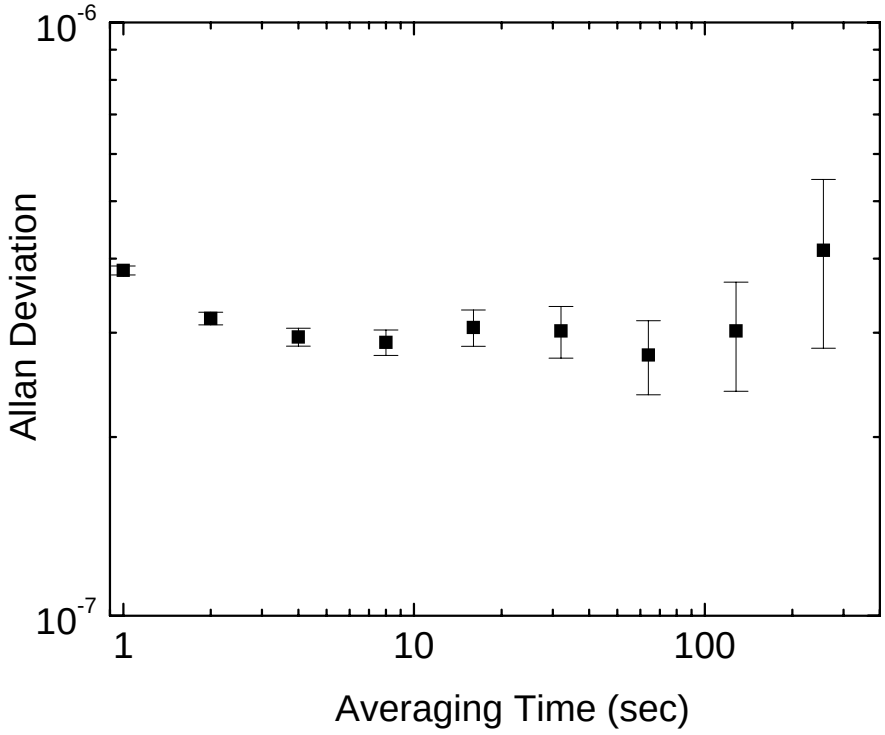

Figure 4.13. Allan deviation of the 419 MHz frequency modulation phase-locked loop (FM PLL). The Allan deviation of the 419 MHz FM PLL versus averaging time, calculated from frequency data over the course of one hour, is shown here. The error bar in each data point represents the one-standard-deviation confidence interval of the Allan deviation.

4.5 Comparison with Local Oscillator Requirement of Chip Scale Atomic Clock

The chip scale atomic clock is the vapor cell atomic clock, scaled down to microelectronic chip size.[6] The operation of CSAC requires a LO to interrogate the atomic transitions to provide the frequency precision. The frequency reference configuration consists of the physics package, the control circuitry, and the LO. In the physics package, the hyperfine transition of the atoms in the vapor cell is induced by a vertical cavity surface emitting laser (VCSEL), modulated at microwave frequency. The optical transmission is subsequently sensed by a semiconductor detector to produce a microwave signal, which is phase locked to the LO to optimize the long term and short term frequency stabilities through the control circuitry. Due to their small size and low operating power, NEMS oscillators are very promising candidates as the LO for CSAC, so it is interesting to compare our achieved noise floor with the LO requirement and evaluate their viability for such applications.

Kitching calculates the LO requirement by demanding that the fractional frequency instability of the CSAC satisfy the DAPRA program goal of 10^{-11} for one hour averaging time.[5] Figure 4.14 shows the phase noise floor of the LO requirement using the hyperfine transitions of Rb^{87} at frequency 6.8 GHz together with the measured phase noise spectra of all the phase-locked loops presented so far, properly scaled to 6.8 GHz. Although the high frequency (>20 kHz) and low frequency (<0.5 Hz) ends of the spectra barely meet the requirement, the middle band between 0.5 Hz and 20 kHz is still 40 dB higher than the requirement. This is due to extrinsic transducer amplifier noise in our still unoptimized experimental configuration. Also shown in figure 4.14 are the projected phase noise spectra of 400 MHz NEMS-based oscillators with $Q = 10^4$ and $Q = 10^5$,

limited by thermomechanical noise at room temperature. They are certainly able to meet the requirements of CSAC with at least 30 dB margin at all frequencies.

Figure 4.15 shows the corresponding Allan deviations of all phase-locked loops versus averaging time τ_A, and the LO requirement. For τ_A longer than 1 sec, all the experimentally achieved Allan deviations already meet the LO requirement. For $\tau_A < 1$ sec, the only available Allan deviation data for the 419 MHz PLL exhibits $1/\sqrt{\tau_A}$ dependence on the averaging time, which is worse than the LO requirement. Also shown in figure 4.15 are the projected Allan deviations of 400 MHz NEMS-based oscillators for Q=10^4 and Q=10^5, limited by thermomechanical noise at room temperature. They are certainly able to meet the LO requirement for all averaging times ranging from 10^{-7} sec to 100 sec. Meeting the LO requirement in terms of both phase noise spectra and Allan deviations clearly demonstrate the viability of the NEMS oscillators as the LO for CSAC.

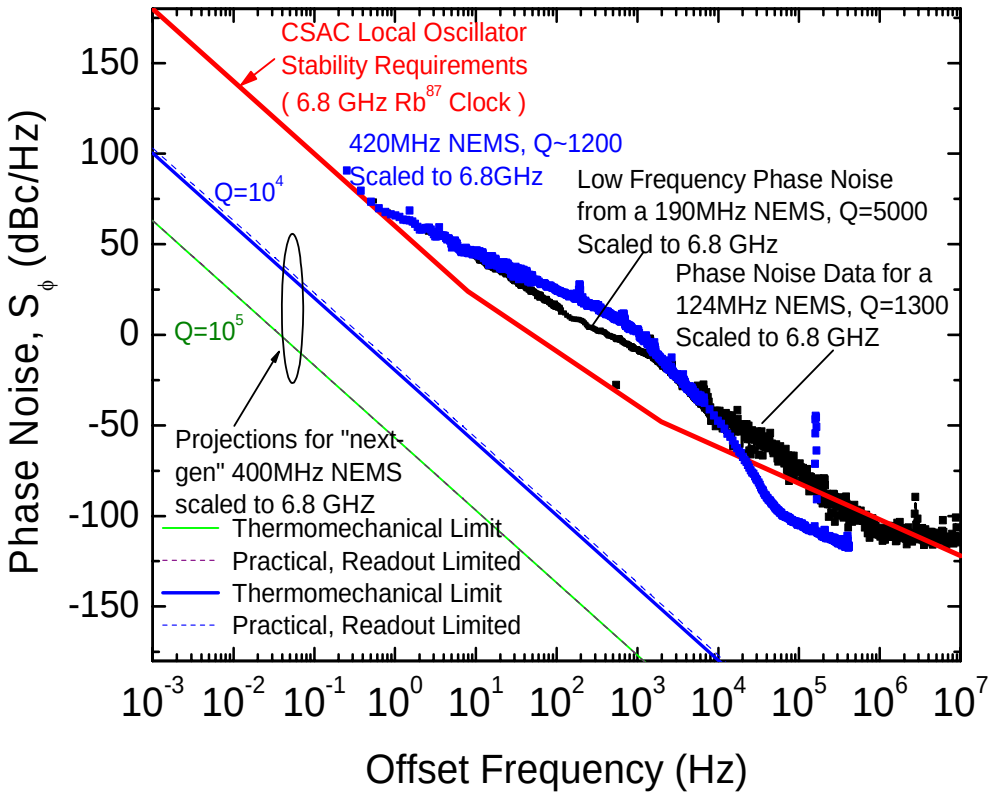

Figure 4.14. Phase noise spectrum of NEMS-based phase-locked loops versus the local oscillator (LO) requirement of chip scale atomic clock (CSAC). The measured phase noise spectra of 125 MHz, 190 MHz and 419 MHz phase-locked loops based on NEMS are compared to the LO requirement of CSAC, upon proper scaling to 6.8 GHz. The projected phase noise spectra of 400 MHz NEMS oscillators with Q=10^4 and Q=10^5, limited by thermomechanical fluctuations at room temperature, clearly shows the ability to meet the CSAC requirement.

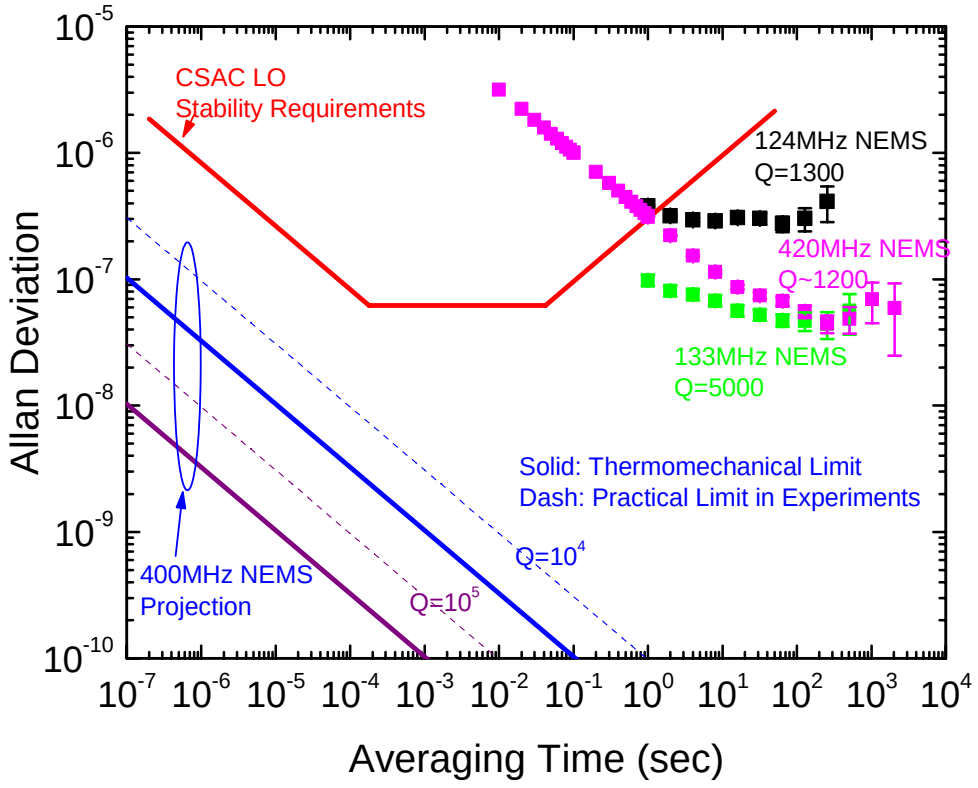

Figure 4.15. Allan deviations of NEMS-based phase-locked loops versus the local oscillator (LO) requirement of chip scale atomic clock (CSAC). The measured Allan deviations of 125 MHz, 190 MHz and 419 MHz phase-locked loops based on NEMS are compared to the LO requirement of CSAC. The projected Allan deviations of 400 MHz oscillators based on NEMS of Q=10^4 and Q=10^5, limited by thermomechanical fluctuations at room temperature, clearly meet the LO requirement of CSAC.

4.6 Experimental Measurement of Diffusion Noise

We have analyzed many noise processes in detail in chapter 3. All these noise processes arise from local fluctuation of the intrinsic thermodynamic properties of a physical system in equilibrium.[7] Although these fluctuations become noise which limits NEMS performance as sensors or resonators, they also provide a potential source of information.[8,9] The fluctuation around the thermodynamic mean is proportional to the number of independent accessible degree of freedom. Moreover, the spectral density of fluctuations is precisely governed by the dynamic parameters of the systems as generally expressed by the fluctuation-dissipation theorem.[7] In particular, when gaseous species adsorb on a NEMS device, typically from the surrounding environment, they can diffuse along the surface in and out of the device. Thus the number of adsorbed atoms in the device can fluctuate, which translates into mass fluctuation and hence frequency fluctuations. The noise spectrum in this case is governed by the diffusion time. We have proposed the diffusion noise theory of NEMS in section 3.5. Here we demonstrate the experimental measurement of the diffusion noise arising from adsorbed xenon atoms on NEMS surface.

We incorporate the NEMS device into a low-noise FM PLL circuit (see section 4.4). Data are obtained from a NEMS resonator with fundamental resonant frequency f_0~190 MHz and dimensions, 2.3 μm (L) × 150 nm (w) × 100 nm (t). (The surface area of the device is A_D=3.45x10^{-13} m^2.) The device is a doubly clamped beam patterned from SiC epilayers[4] and capped with thermally evaporated dual metallic layers: 30 nm Al (bottom) and 5 nm Ti (top). (The effective vibratory mass of the device, including the metallic layers, is M_{eff}=96 fg.) After fabrication, the device is loaded into a UHV

cryostat, actuated magnetomotively,[4] and exhibits Q of ~5000 for the fundamental in-plane flexural mode of vibration at the measurement temperatures ~58 K.

Xenon is used in our experiments due to its large atomic mass (m_{Xe}=130 amu), and its well characterized surface behavior in literature.[10-14] A gas nozzle is used to deliver a constant, calibrated flux to the device (see also section 5.2). The flux to the device, Φ, is 2.65×10^{17} atom/m^{2}sec, corresponding to an effective pressure of 6.6×10^{-8} torr at 58 K. Data presented here are taken at constant flux, while changing the temperature of the device.

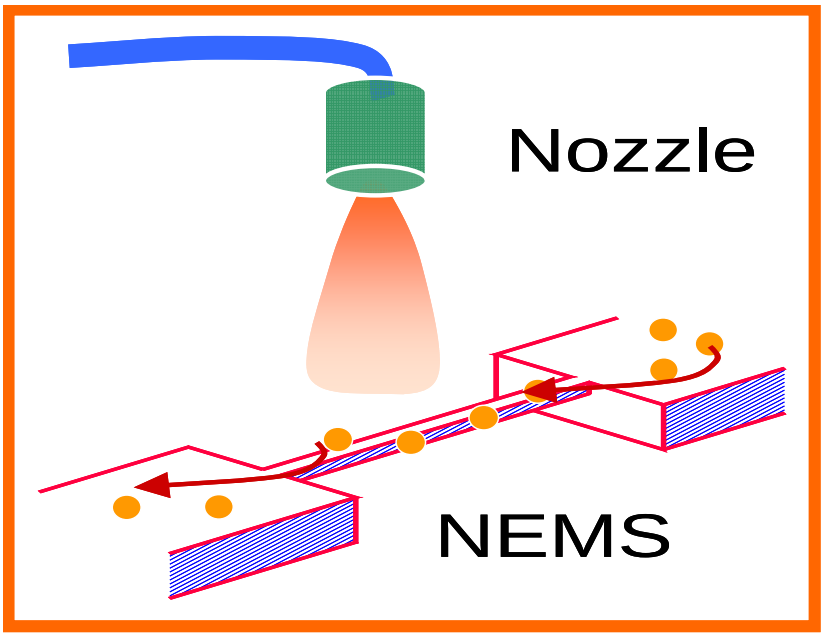

Figure 4.16. Experimental configuration for diffusion noise measurement. A gas nozzle with a 300 μm aperture provides a controlled flux of atoms or molecules. The flux is determined by direct measurements of the gas flow rate, in conjunction with a well-validated model for the molecular beam emanating from the nozzle.

First, we measure the adsorption spectrum, defined as the total number of adsorbed xenon atoms versus temperature. As the device is cooled below 57 K, we observe irreversible accumulation of xenon in solid phase due to the two-dimensional solid-gas phase transition.[11] The adsorption of xenon is fully reversible above this transition temperature. All the measurements are thus done above 57 K. We take the resonance frequency data of the device versus temperature with applied flux and without flux, denoted by $f_G(T)$ and $f_{NG}(T)$, respectively. The adsorption spectrum is deduced from the frequency change by $N(T) = -m_{Xe}(f_G(T) - f_{NG}(T)/(\Re/2\pi)$ due to the presence of gas, where $\Re/2\pi = f_0/2M_{eff} = 0.99$ Hz/zg is the mass responsivity of the device.[15] The coverage θ, defined as the number of adsorbed atoms per unit area, i.e., $N(T)/A_D$, is 6.67×10^{14} atoms/cm^2 at T=58 K, consistent with a commensurate monolayer coverage of 5×10^{14} atoms/cm^2 on Pt(111) at T=85 K.[13] Because the roughness of thermally evaporated Ti top layer of the device completely blurs the monolayer transition of xenon, we do not observe such a transition in the adsorption spectrum.[2]

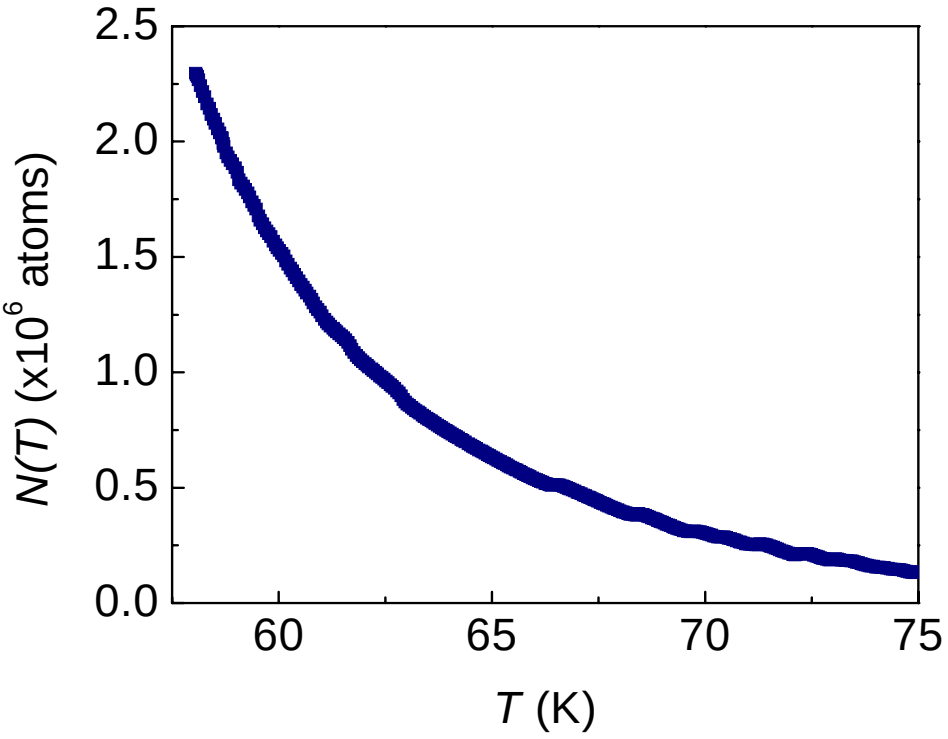

Figure 4.17. Adsorption spectrum of xenon atoms on NEMS surface. The adsorption spectrum is deduced from $N(T) = -m_{Xe}(f_G(T) - f_{NG}(T)/(\Re/2\pi)$, $\Re/2\pi = 0.99$ Hz/zg is the mass responsivity of the device. $f_G(T)$ and $f_{NG}(T)$ denote the resonant frequency data with applied gaseous flux and no flux, respectively.

Figure 4.18 shows the representative data of the spectral density of fractional frequency noise at T= 58 K with and without gaseous flux. The spectrum with no applied flux exhibits flicker noise from 0.1 Hz to 2 Hz and flattens out above 2 Hz, reflecting the instrumentation noise of FM PLL. In contrast, the spectrum with applied flux clearly shows excess noise contribution from gas. We have of course tested that the parameters affecting the loop gain of FM PLL (in particular, the quality factor of the resonator) do not change with temperature or coverage, and therefore cannot be responsible for the excess noise. More quantitatively, we calculate the fractional frequency noise contributed from gas, $S_y^G(\omega)$, by subtracting the spectral density of fractional frequency noise with zero flux, $S_y^{NG}(\omega)$, from that with applied flux at given temperatures $S_y^{Total}(\omega)$, i.e., from the formula $S_y^G(\omega) = S_y^{Total}(\omega) - S_y^{NG}(\omega)$. All the resulting spectra, as shown in figure 4.19, exhibit predicted functional form from equation (3.53), i.e.,

$$S_y(\omega) = \frac{aN(T)}{4\pi}\left(\frac{m_{Xe}}{M_{eff}}\right)^2 \int_0^\infty \frac{\cos\omega\tau}{(1+\tau/\tau_D)^{1/2}}\, d\tau . \qquad (4.18)$$

These spectral data are fitted to extract the diffusion time τ_D, using equation (4.18). Because the extracted diffusion times, ranging from 0.114 sec to 0.053 sec, are much shorter than the typical correlation times of an adsorption-desorption cycle,[16] the observed noise spectra cannot be attributed to adsorption-desorption process.

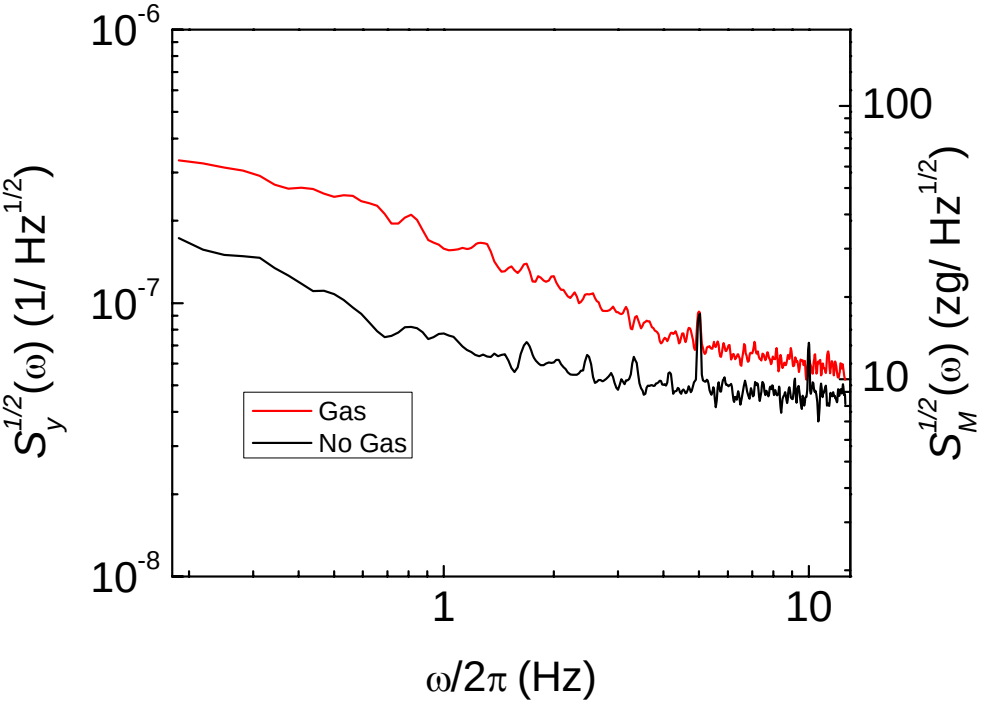

Figure 4.18. Representative fractional frequency noise spectra. The spectral density of fractional frequency with and without gaseous flux at T=59.2 K is shown. The spectrum, $S_y^{NG}(\omega)$, with no applied flux (black) reflects the instrumentation noise of FM PLL. In contrast, the spectrum $S_y^{Total}(\omega)$ with applied flux (red) clearly shows excess noise contribution from gas. The right hand axis shows the scale of the corresponding mass fluctuations in unit of zg/Hz$^{1/2}$.

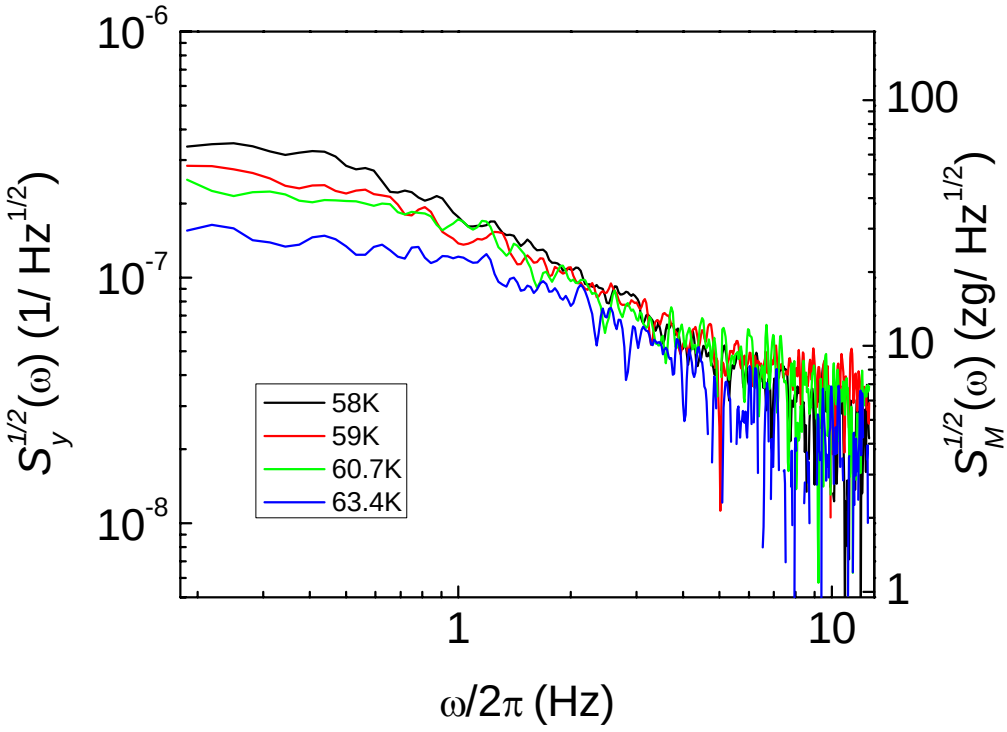

Figure 4.19. Spectral density of fractional frequency noise contributed from gas. The spectral density of fractional frequency noise contributed from the gaseous flux at four measurement temperatures is displayed. We calculate the fractional frequency noise contributed from gas, $S_y^G(\omega)$, by subtracting the spectral density of fractional frequency noise with zero flux, $S_y^{NG}(\omega)$, from that with applied flux at given temperatures $S_y^{Total}(\omega)$, i.e., from the formula $S_y^G(\omega) = S_y^{Total}(\omega) - S_y^{NG}(\omega)$. The right hand axis shows the scale of the corresponding mass fluctuations in unit of zg/Hz$^{1/2}$.

From the diffusion noise theory, we can also calculate the diffusion coefficients D by $D = L^2/(2a^2\tau_D)$, where a=4.43 is a numerical factor, and L=2.3 μm is the device length, (see section 3.5). Table 4.3 lists the extracted diffusion times and diffusion coefficients together with the corresponding coverage at four measurement temperatures. In general, the surface diffusion of xenon is determined by the corrugation of the adsorbate-surface potential and the attractive interactions between the adsorbed atoms.[13] At very dilute limits, the xenon atoms behave and diffuse like an ideal two-dimensional gas.[10,12] At higher coverage, however, the diffusion is more dominated by the attractive interaction between the adsorbed xenon atoms and as a result, the diffusion coefficient dramatically decreases with increasing coverage.[13] Our extracted diffusion coefficients are very close to D=2x10^{-8} cm^2/s, reported by Meixner and George for xenon on Pt(111) for coverage $\theta = 5\text{x}10^{14}$ atoms/cm^2 in spite of very different surface conditions and measurement temperatures.[13] The indifference of the diffusion coefficients to surface conditions and temperatures suggests that in both cases the attractive interaction between adsorbed xenon atoms completely dominates the surface diffusion.

Figure 4.21 shows the measured Allan deviation $\sigma_A(\tau_A)$ versus temperature with and without the gaseous flux for averaging time τ_A= 1 sec. The Allan deviation with zero applied flux, denoted by σ_A^{NG}, reflects the instrumentation noise floor of the FM PLL and slightly decreases with temperature. We attribute this slight decreasing trend with temperature to the corresponding increase in quality factor (15%) from T=75 K to T=58 K. In contrast, for temperature below 65 K, the Allan deviation with gaseous flux, σ_A^{Total}, clearly exceeds the instrumentation noise floor due to the excess noise contribution from the gas. Figure 4.22 shows the Allan deviation contributed from gas, σ_A^G, calculated by

subtracting the Allan deviation without gas from Allan deviation with gas, i.e., from the formula $(\sigma_A^G)^2 = (\sigma_A^{Total})^2 - (\sigma_A^{NG})^2$.

From equation (3.58), the expression for Allan deviation from diffusion noise theory is

$$\sigma_A^2(\tau_A) = \int_0^\infty \frac{8}{(\omega\tau_A)^2} S_y(\omega)\sin^4(\omega\tau_A/2)d\omega = \frac{2aN(T)}{\pi}\left(\frac{m_{Xe}}{M_{eff}}\right)^2 X(\frac{\tau_D}{\tau_A}), \tag{4.19}$$

where $X(\tau_D/\tau_A)$ is a function defined in equation (3.59). Equation (4.19) shows that Allan deviation associated with the number fluctuation of an ensemble of adsorbed atoms is proportional to the square root of its total number, $N(T)$. Roughly speaking, we can thus attribute the monotonically increasing trend in Allan deviation in figure 4.22, as temperature is lowered, to the corresponding increase in the number of adsorbed xenon atoms in figure 4.17. Using equation (4.19) and measured $N(T)$ and τ_D from table 4.3, we calculate the Allan deviation and display the result in figure 4.22. In figure 4.22, we also show the calculated Allan deviation, $\sigma_A(\tau_A) = \sqrt{N_a}\sigma_{OCC}(m_{Xe}/M_{eff})\sqrt{\tau_A/6\tau_r}$, from Yong and Vig's model for the case of immobile monolayer adsorption, assuming the monolayer coverage N_a = 2.3x10^6 at T=58 K and the sticking coefficient s=1 to estimate the correlation time for an adsorption-desorption cycle from $\tau_r = N(T)/(\Phi s A_D)$ and the variance of occupational probability from $\sigma_{OCC}^2 = N(N_a - N)/N_a^2$ (see section 3.4).[17,18] As shown in figure 4.22, the experimentally observed Allan deviation is consistent with the prediction from diffusion noise theory. In contrast, the estimated Allan deviation from Yong and Vig's model, vanishing at completion of one monolayer, is apparently contradictory to experimental observation.

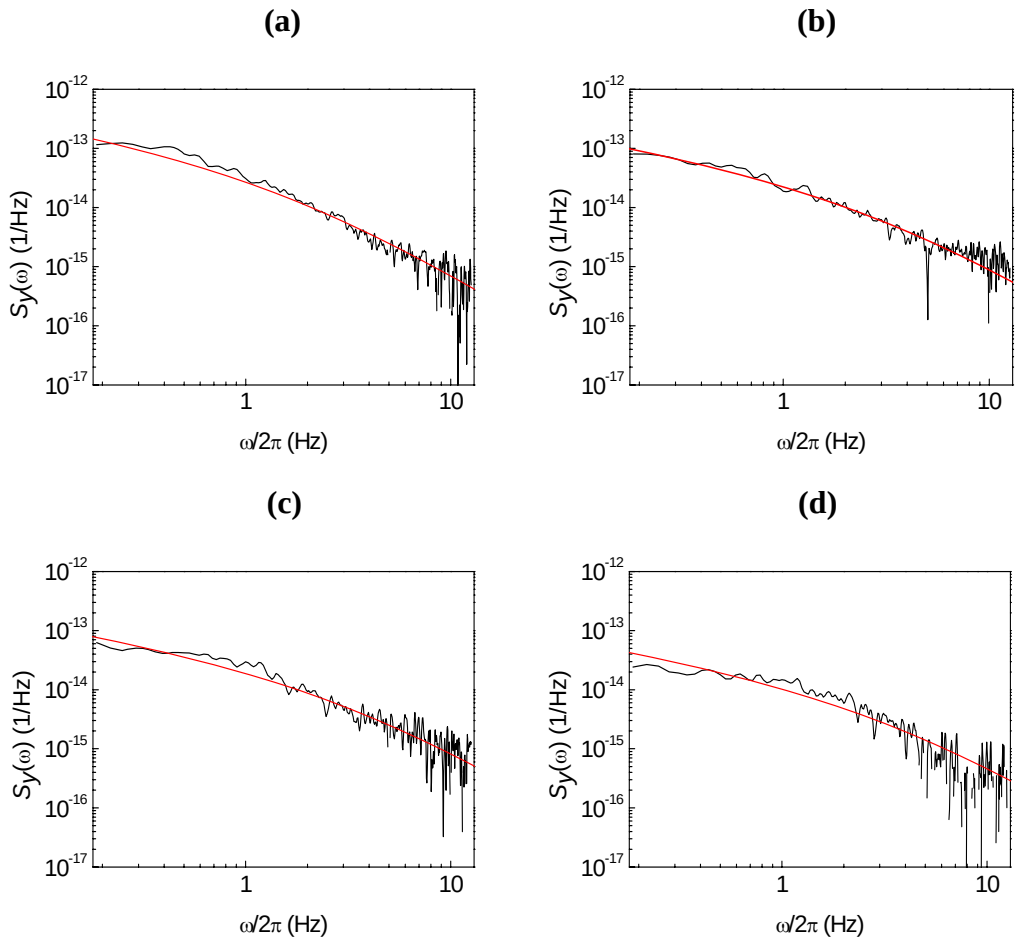

Figure 4.20. Spectral density of fractional frequency noise with fitting. Data (black) from figure 4.19 are fitted by a predicted function form in equation (4.18) (red) from diffusion noise theory to extract the diffusion times. **(a) Spectral density data with fitting at *T*= 58 K. (b) Spectral density data with fitting at *T*=59.2 K. (c) Spectral density data with fitting at *T*=60.7 K. (d) Spectral density data with fitting at *T*=63.4 K.**

Temp	N	θ	τ_D	D
K	atom	atom/cm^2	sec	cm^2/sec
58	2.30×10^{6}	6.67×10^{14}	0.114	1.15×10^{-8}
59.2	1.79×10^{6}	5.19×10^{14}	0.0637	2.06×10^{-8}
60.7	1.33×10^{6}	3.86×10^{14}	0.0553	2.37×10^{-8}
63.4	8.08×10^{5}	2.34×10^{14}	0.0530	2.47×10^{-8}

Table 4.3. Summary of diffusion times and coefficients versus temperature

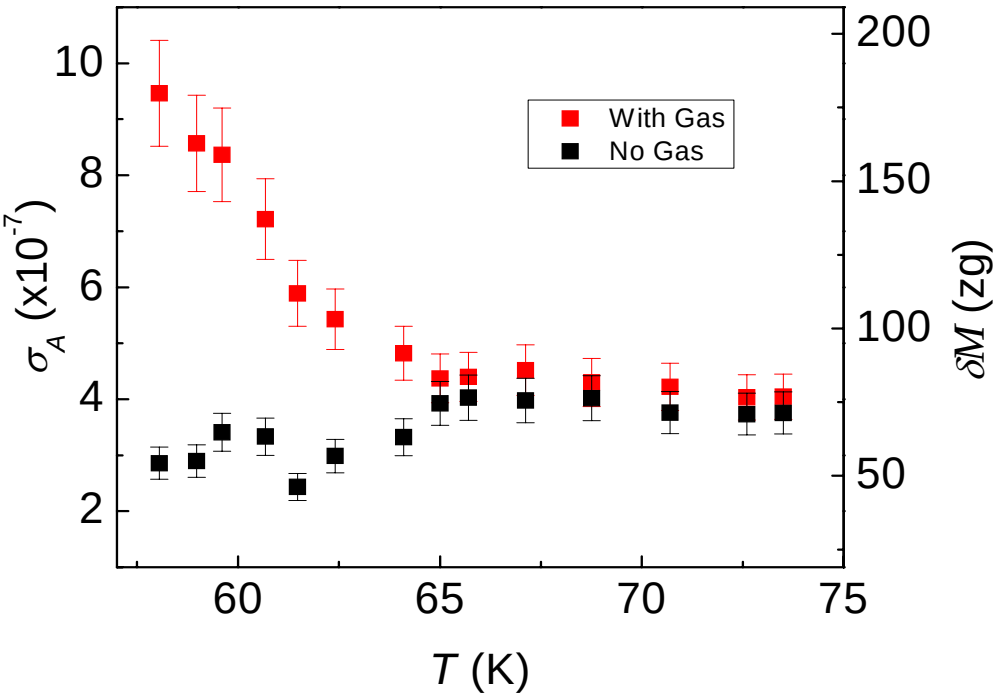

Figure 4.21. Allan deviation data with gas and without gas. The Allan deviation (black) with zero applied flux reflects the instrumentation noise floor of the FM PLL. For temperature below 65 K, the Allan deviation (red) with gas clearly exceeds that without gas due to the excess noise contribution from the gas. The right-hand axis shows the scale of the corresponding mass fluctuation in units of zg.

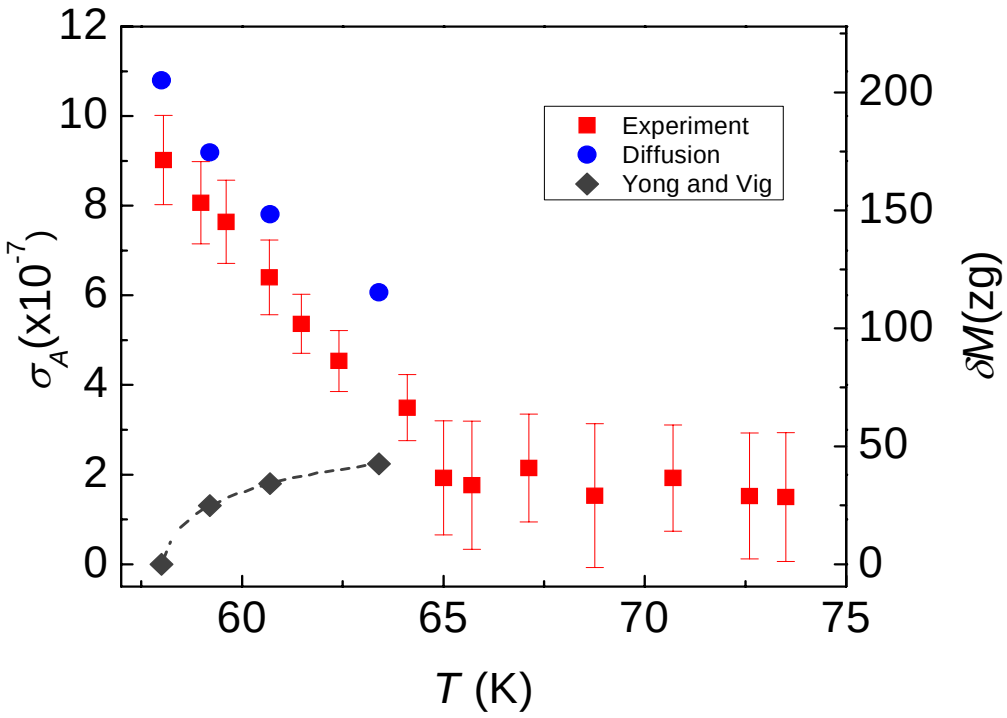

Figure 4.22. Comparison with prediction from diffusion noise theory and Yong and Vig's model. The Allan deviation (red) contributed from gas, σ_A^G, is calculated by subtracting the Allan deviation without gas from Allan deviation with gas, i.e., from the formula $(\sigma_A^G)^2 = (\sigma_A^{Total})^2 - (\sigma_A^{NG})^2$. The Allan deviation (blue) from diffusion noise is calculated using equation (4.19) and measured $N(T)$ and τ_D from table 4.3. For comparison, the calculated Allan deviation (dark gray) from Yong and Vig's model is also displayed, assuming the monolayer coverage N_a = 2.3x10^6 at T=58 K and the sticking coefficient s=1. The right hand axis shows the scale of the corresponding mass fluctuation in units of zg.

As already mentioned, no appreciable change in quality factor is observed from the adsorbed species in our experiment and thus the observed diffusion noise is non-dissipassive in nature, a very important attribute of parametric noise as pointed out by Cleland and Roukes.[17]

Having verified that the observed fluctuations are due to the mass fluctuation caused by diffusion, we can relate the spectral density of mass fluctuation $S_M^{1/2}(\omega)$ to the spectral density of fractional frequency noise $S_y^{1/2}(\omega)$ by the expression $S_M^{1/2}(\omega) = f_0 S_y^{1/2}(\omega)/(\Re/2\pi)$ with the mass responsivity. Similarly, we relate the Allan deviation to the corresponding mass fluctuation δM by $\delta M = f_0 \sigma_A /(\Re/2\pi)$. The scale in the right hand axes in figure 4.18, 4.19, 4.21 and 4.22 shows that the corresponding mass fluctuation is on the order of tens of zeptogram (1 zeptogram = 10^{-21} gram) and thus our experiment is indeed the "fluctuation sensing" at zeptogram scale.

4.7 Conclusion

In this chapter, we present the experimental measurement of phase noise of NEMS. We first analyze control servo behavior of a phase-locked loop based on NEMS and give the expressions for the locked condition and measurement bandwidth. Based on such a scheme, we then present in detail several electronic implementations, all of which are designed to lock minute mechanical resonance of NEMS and complement each other in their merits. The homodyne phase-locked loop based on a two-port NEMS device fully utilizes the intrinsic bandwidth provided by NEMS, and is very desirable for sensing applications requiring fast response time. It requires, however, laborious manual adjustments and is limited in the locking range. On the other hand, the FM PLL, touted

for its easy loop implementation and large locking range, suffers from the limited bandwidth due to the lock-in detection. In general, the observed Allan deviation $\sigma_A(\tau_A)$ is consistent with the estimated value from the expression $\sigma_A(\tau_A) = (1/Q)10^{-DR/20}$ with experimentally determined dynamic range *DR* and *Q*. We summarize the performance of all the phase-locked loops with their device parameters considered in this chapter in table 4.1.

We then consolidate the phase noise and Allan deviation data of all the phase-locked loops and compare them with the LO requirement of CSAC. While our current performance, limited by transducer amplifier noise, only partially meets the requirement, the projected phase noise and Allan deviation for 400 MHz NEMS based oscillators with Q=10^4 and Q=10^5, limited by thermomechanical noise, clearly show the potential for this application.

We further demonstrate the measurement of diffusion noise arising from adsorbed xenon atoms on the NEMS device. In general, our experimental results can be explained with the diffusion noise theory. The measured spectra of fractional frequency noise confirm the predicted functional form from the diffusion noise theory and the extracted diffusion coefficients agree well with the reported values in literature. Moreover, the measured Allan deviation contributed from gas is consistent with the theoretical estimates from diffusion noise theory, using the total number of adsorbed atoms and extracted diffusion times. Finally, we point out that the diffusion noise or its equivalent mass fluctuation, measured with unprecedented mass sensitivity at zeptogram level, imposes the ultimate sensitivity limits of any nanoscale gas sensors, regardless of their sensing mechanisms. But more importantly, this work, for the first time, goes beyond simple

measurement of adsorption spectrum in nanodevices and demonstrate a canonical example where a high quality factor NEMS device, inserted into a phase-locked loop, serves to probe the noise process of the adsorbed species and extract the microscopic and dynamic information of surface diffusion. We expect the generalization of this approach will find many interesting applications in surface science of nanodevices.

References

1. H. Pauly and G. Scoles (editor) *Atomic and Molecular Beam Methods* (New York, Oxford University Press, 1988).

2. J. Krim, D. H. Solina, and R. Chiarello Nanotribology of a Kr Monolayer: a quartz-crystal microbalance study of atomic scale friction. *Phys. Rev. Lett*. **66**, 181-184 (1991).

3. T. R. Albrecht, P. Grutter, D. Horne, and D. Rugar Frequency modulation detection using high Q cantilever for enhanced force microscopy sensitivity. *J. Appl. Phys.* **69**, 668 (1991).

4. Y. T. Yang, K. L. Ekinci, X. M. H. Huang, M. L. Roukes, C. A. Zorman, and M. Mehregany Monocrystalline 3C-SiC nanoelectromechanical systems. *Appl. Phys. Lett.* **78**, 612 (2001).

5. J. Kitching Local oscillator requirements for chip-scale atomic clocks. *Private communication* (2004).

6. J. Kitching, S. Knappe, and L. Hollberg Miniatured vapor-cell atomic frequency. *Appl. Phys. Lett.* **81**, 553 (2002).

7. L. D. Landau and E. M. Lifshitz *Statistical Physics* Vol. 1 (Oxford, Butterworkth-Heinemann,1980).

8. E. L. Elson and D. Magde Fluoresence correlation spectroscopy I concept basis and theory. *Biopolymer* **13**, 1-27 (1974).

9. D. Magde, E. L. Elson, and W. W. Webb Thermodynamic fluctuations in a reacting system- Measurement by fluorescence correlation spectroscopy. *Phys. Rev. Lett.* **29**, 705-708 (1972).

10. C. T. Rettner, D. S. Bethune, and E. K. Schweizer Measurement of Xe desorption rates from Pt(111):Rates for an ideal surfaces and in the defect-dominated regime. *J. Chem. Phys.* **92**, 1442 (1990).

11. H. Clark *The theory of Adsorption and Catalysis* (London, Academic Press, 1970).

12. J. Ellis, A. P. Graham, and J. P. Toennies Quasielastic helium atom scattering from a two-dimensional gas of xenon atoms on Pt(111). *Phys. Rev. Lett.* **82**, 5072-5075 (1999).

13. D. L. Meixner and S. M. George Surface diffusion of xenon on Pt(111). *J. Chem. Phy.* **98**, 11 (1983).

14. H. J. Kreuzer and Z. W. Gortel *Physisorption Kinetics* (Heidelberg, Springer-Verlag, 1986)

15. K. L. Ekinci, Y. T. Yang, and M. L. Roukes Ultimate limits to inertial mass sensing based upon nanoelectromechanical systems. *J. Appl. Phys.* **95**, 2682 (2004).

16. To measure the correlation time of an adsorption desorption cycle, we dose the device with given coverage, block the gaseous flux with mechanical shutter, and observe the coverage over the time. Under similar conditions, the typical correlation time, obtained by fitting the exponential decay of the coverage, is >2 sec.

17. A. N. Cleland and M. L. Roukes Noise processes in nanomechanical resonators. *J. Appl. Phys.* **92**, 2758 (2002).

18. Y. K.Yong and J. Vig Resonator surface contamination: a cause of frequency fluctuations. *IEEE Trans. On Ultrasonics, Ferroelectric, and Frequency Control* **36**, 452 (1989).